ELSEVIER

Thickness distribution of a cooling pyroclastic flow deposit on Augustine Volcano, Alaska: Optimization using InSAR, FEMs, and an adaptive mesh algorithm

Timothy Masterlark [a,*], Zhong Lu [b], Russell Rykhus [b]

[a] *Department of Geological Sciences, University of Alabama, Tuscaloosa, AL 35487, United States*
[b] *USGS National Center for EROS, SAIC, Sioux Falls, SD 57198, United States*

Abstract

Interferometric synthetic aperture radar (InSAR) imagery documents the consistent subsidence, during the interval 1992–1999, of a pyroclastic flow deposit (PFD) emplaced during the 1986 eruption of Augustine Volcano, Alaska. We construct finite element models (FEMs) that simulate thermoelastic contraction of the PFD to account for the observed subsidence. Three-dimensional problem domains of the FEMs include a thermoelastic PFD embedded in an elastic substrate. The thickness of the PFD is initially determined from the difference between post- and pre-eruption digital elevation models (DEMs). The initial excess temperature of the PFD at the time of deposition, 640 °C, is estimated from FEM predictions and an InSAR image via standard least-squares inverse methods. Although the FEM predicts the major features of the observed transient deformation, systematic prediction errors (RMSE=2.2 cm) are most likely associated with errors in the a priori PFD thickness distribution estimated from the DEM differences. We combine an InSAR image, FEMs, and an adaptive mesh algorithm to iteratively optimize the geometry of the PFD with respect to a minimized misfit between the predicted thermoelastic deformation and observed deformation. Prediction errors from an FEM, which includes an optimized PFD geometry and the initial excess PFD temperature estimated from the least-squares analysis, are sub-millimeter (RMSE=0.3 mm). The average thickness (9.3 m), maximum thickness (126 m), and volume (2.1×10^7 m³) of the PFD, estimated using the adaptive mesh algorithm, are about twice as large as the respective estimations for the a priori PFD geometry. Sensitivity analyses suggest unrealistic PFD thickness distributions are required for initial excess PFD temperatures outside of the range 500–800 °C.
© 2005 Elsevier B.V. All rights reserved.

Keywords: finite element analysis; interferometry; deformation; thermoelastic properties; volcano

1. Introduction

Interferometric synthetic aperture radar (InSAR) imagery can map incremental deformation that occurs during a time interval. Analyses of InSAR

---

* Corresponding author. Tel.: +1 205 348 5095.
  E-mail address: masterlark@geo.ua.edu (T. Masterlark).

imagery have documented deformation associated with a wide variety of geomechanical phenomena, such as glacier movements (Stenoien and Bentley, 2000), coseismic slip (Massonnet et al., 1993), post-seismic relaxation (Pollitz et al., 2001), poroelastic rebound (Peltzer et al., 1996), cooling lava (Stevens et al., 2001), and magma intrusion (Masterlark and Lu, 2004). InSAR imagery has been especially useful for studying volcanoes that are restless but poorly instrumented because of their remote locations (Lu et al., 2003b). Volcano deformation attributed to magmatic unrest is often a precursor for eruptive activity (Lipman et al., 1981; Lu et al., 2003a). Combinations of InSAR imagery and numerical modeling can differentiate between magmatic activity and other deformation mechanisms (Lu et al., 2002; Masterlark and Lu, 2004) and are therefore powerful volcano hazards assessment tools.

InSAR imagery indicates that the north flank of Augustine Volcano, Alaska, was actively deforming during 1992–1999 (Lu et al., 2003b). This region of deformation corresponds to the spatial extent of the pyroclastic flow deposit (PFD) emplaced during the 1986 eruption of Augustine Volcano. We attribute this deformation to post-emplacement behavior of the PFD. Consistent with other geodetic observations of the volcano (Pauk et al., 2001), volcano-wide deformation attributed to possible magmatic activity is not observed with InSAR images spanning 1992–1999.

This study is concerned with quantifying the post-eruption deformation of the PFD emplaced during the 1986 eruption of Augustine Volcano. We construct finite element models (FEMs) that simulate the post-eruptive thermoelastic contraction of the initially hot and geometrically complex PFD. Results of this study indicate that *(1)* InSAR imagery documents the systematic post-emplacement subsidence of the PFD; *(2)* linear thermoelastic behavior, which simulates the cooling PFD, can account for the observed deformation; and *(3)* a technique combining InSAR imagery, FEMs, and an adaptive mesh algorithm can optimize the poorly constrained geometry of the PFD. This optimization generates a PFD thickness distribution map derived from remote sensing data and linear thermoelastic deformation mechanics.

2. Augustine Volcano

Augustine Volcano forms a 92 km^2 island in the southwest end of Cook Inlet, Alaska (Fig. 1). Augustine's volcanism began in the late Pleistocene and the volcano is the youngest (Miller et al., 1998) and most active of the four volcanoes (Spurr, Redoubt, Iliamna, and Augustine) that form a line roughly parallel to Cook Inlet. The maximum elevation is currently about 1250 m above sea level. However,
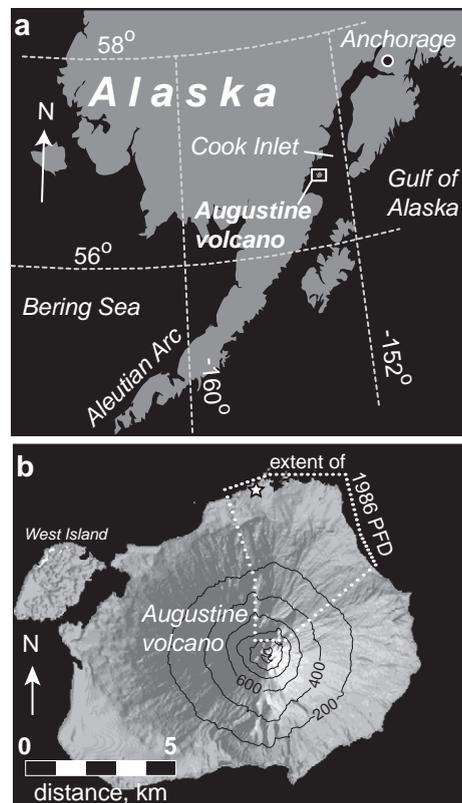

Fig. 1. Study site. (a) Location. Augustine Volcano is an island located in the southwest part of Cook Inlet, Alaska. (b) Shaded relief image of Augustine Volcano. The shaded relief image is constructed from a post-1986 eruption digital elevation model. The terrestrial area of the volcano, including West Island, is 92 km^2. The 200 m contour intervals reveal the overall symmetry of the volcano. The asymmetric regions along the coastal margin are due to episodic debris avalanches (Begét and Kienle, 1992). The white dots outline the assumed spatial extent of the 1986 PFD. The star near the upper left corner of the PFD marks the location of wave cut exposures and the embedded aluminum float used for in situ temperature and density experiments (Begét and Limke, 1989).

the summit elevation and morphology fluctuate significantly during eruptions due to a combination of lava dome growth and explosive removal (Swanson and Kienle, 1988). The volcano's structure consists of a dome and lava flow complex surrounded by an assembly of ash, lahar, avalanche, and PFD deposits (Begét and Kienle, 1992; Miller et al., 1998; Waythomas and Waitt, 1998). The primarily andesitic composition of Augustine Volcano accounts for the historically explosive eruption behavior and is comparable to rocks of the other Cook Inlet volcanoes (Miller et al., 1998).

Six documented eruptions occurred in the twentieth century and a similar number of earlier eruptions with ages up to two thousand years have been identified based on carbon dating techniques (Simkin and Siebert, 1994). Hummocky offshore topography, revealed by bathymetry data, reveals the extent of episodic debris flows from the peak of Augustine Volcano (Begét and Kienle, 1992). Water depths surrounding Augustine Volcano are limited to a few tens of meters for offshore distances up to several kilometers. West Island (Fig. 1) is a terrestrial expression of a debris avalanche that extends several kilometers to the northwest of Augustine Volcano.

Others describe the most recent (1986) eruption of Augustine Volcano in detail (e.g., Swanson and Kienle, 1988; Miller et al., 1998; Waythomas and Waitt, 1998) and a summary of the eruption is given here. The 1986 eruption had three major episodes: March 27–April 2, April 23–28, and August 22–September 1. A seismic swarm began five weeks prior to the initial eruption episode. An ash cloud created during the initial eruption episode (March 27–April 2, 1986) reached an altitude of 12,000 m. This episode produced substantial lahar and pyroclastic flows that cover the northern flank of the volcano. The second eruption episode (April 23–28, 1986) produced a small lava flow, pyroclastic flows, and an ash plume that reached an altitude of 3700 m. The third eruption episode (August 22–September 1, 1986) produced a small lava flow, more pyroclastic flows, and a small ash cloud. This final episode culminated with dome building.

PFDs generated from the 1986 eruption blanket a fan-shaped region of the northern flank of Augustine

Volcano (Begét and Limke, 1989). Coverage by the lithic block and ash flow deposits of the PFD is narrow near the peak and widens in the down slope direction. These deposits extend all the way to the coast to the north–northeast of the Peak. Directly to the north of the peak, the lithic block and ash deposits give way to lithic-rich pumice deposits of the PFD, which extend to the coast. Begét and Limke (1989) provide constraints on the emplacement density, temperature, and thickness for a region of the PFD near the coast (Fig. 1b). Based on the submergence of a spherical aluminum fishing float transported on the PFD, they estimate the upper limit for the emplacement density of the PFD is 1360 kg m^{-3}. The submerged region of the float is oxidized and discolored. An in situ field experiment on a portion of the spherical float above the discolored region suggests the initial temperature of the PFD from the 1986 eruption of Augustine Volcano is at least 425 °C. Begét and Limke (1989) also report wave-cut exposures that suggest the PFD thickness near the northern coast is 1 to 2 m.

3. Data

3.1. InSAR images

We construct eighteen InSAR images from synthetic aperture radar image pairs acquired by ERS-1 and ERS-2 C-band (wavelength = 5.66 cm) radar satellites using the two-pass InSAR method described by Massonnet and Feigl (1998). These InSAR images document the surface deformation of Augustine Volcano during 1992–1999 (Fig. 2). Individual images span a variety of roughly annual intervals during this seven-year period (Fig. 3). The InSAR data include five different line-of-sight (LOS) vectors (Table 1) from both ascending and descending passes and reveal systematic changes in range, between the satellites and the land surface, along the north flank of the volcano. This region corresponds to the spatial extent of the PFD emplaced during the 1986 eruption (Fig. 4).

Each InSAR image maps a single, mostly vertical, component of deformation parallel to the corresponding LOS vector. The systematic and positive changes in range shown in all images suggest the PFD is
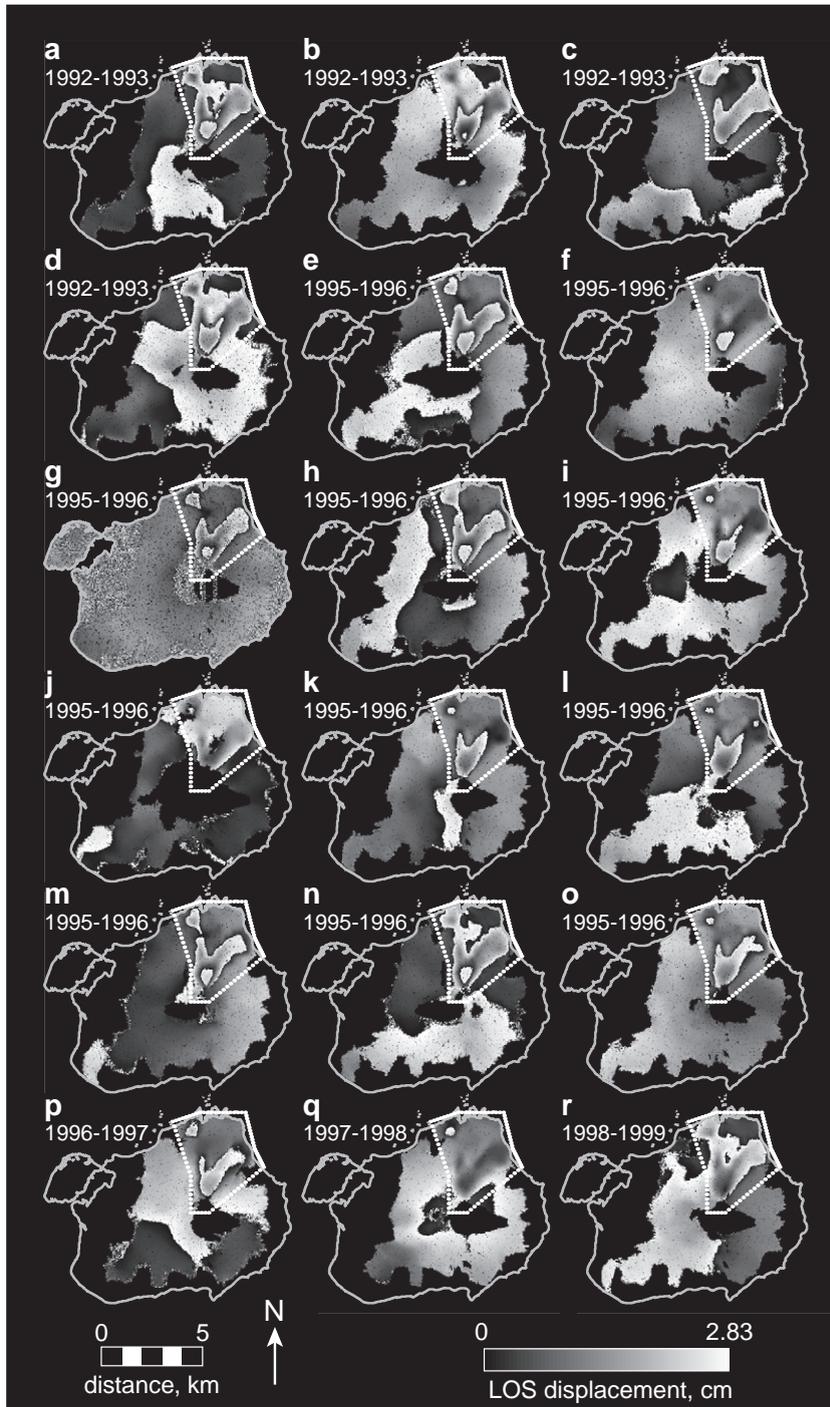
Fig. 2. InSAR images. Eighteen InSAR images document the systematic deformation of the PFD (outlined with white dots) during 1992–1999. The InSAR image at the top left is used to calibrate the FEMs. Each black-gray-white cycle represents 2.83 cm of relative deformation toward the satellite. Table 1 summarizes the specifications for each image.
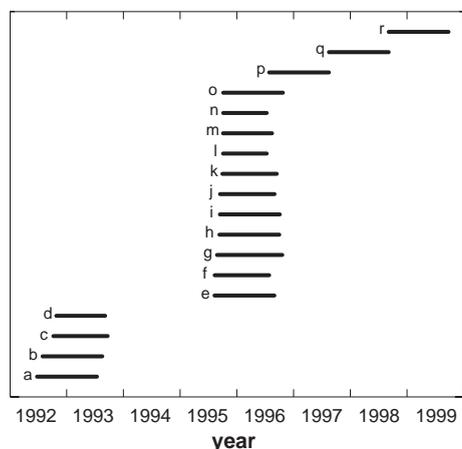
Fig. 3. Temporal coverage of InSAR images. Black bars correspond to the time intervals spanned by each of the InSAR images. The image labeling convention corresponds to that for Fig. 2 and Table 1.

3.2. Thermal image

The multi-spectral image used in this study was acquired during daylight hours on April 28, 1986 by the Landsat 5 Thematic Mapper (TM) sensor. TM data is composed of seven spectral bands. TM bands 1–5 and 7 collect energy reflected from the Earth's surface and have a nominal spatial resolution of 30 m. TM band 6 is an infrared band that collects energy emitted from the Earth's surface and is useful for thermal mapping and estimating soil moisture (Sabins, 1997). Spatial resolution for TM band 6 is 120 m. The TM band 6 image of Augustine Volcano (Fig. 4b) reveals the stark contrast between the bright and therefore relatively hot PFD and the darker and therefore cooler surrounding surface immediately following the second episode of the 1986 eruption.

3.3. Digital elevation models

Two digital elevations models (DEMs) characterize the topography of Augustine Volcano, one before, and one after the 1986 eruption. The pre-1986 DEM is from the US Geological Survey National Elevation Dataset (NED) (Gesch et al., 2002). The horizontal resolution is 60 m and the root-mean-squared-error (RMSE) of vertical elevation is 15 m (Gesch, 1994).

consistently subsiding as much as 3 cm a^{-1} during 1992–1999 (Lu et al., 2003b). Although vertical components dominate the LOS vectors, the other two orthogonal components in each vector are non-zero. For the remainder of this paper, our usage of "subsidence" implies the dominance of vertical deformation, although we quantitatively recognize the horizontal components.

Table 1
InSAR image specifications

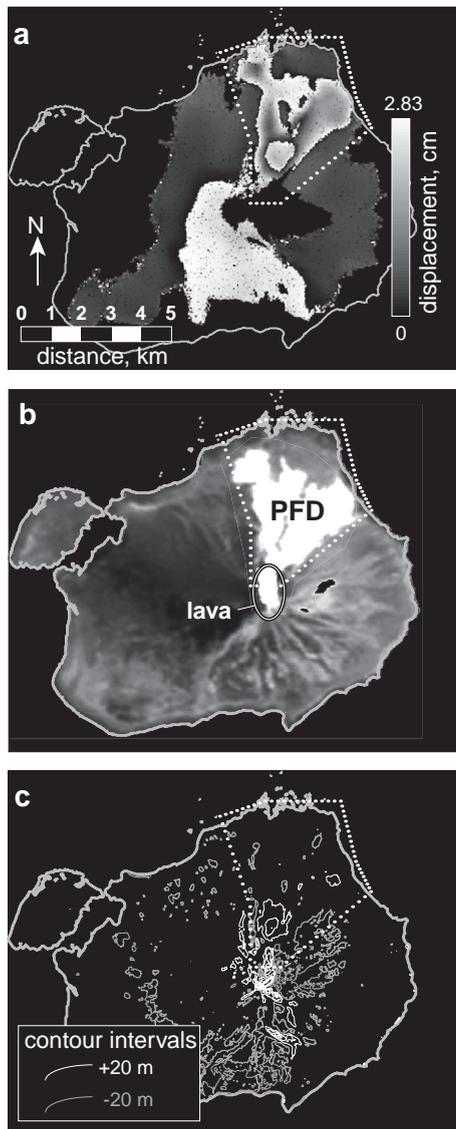| InSAR image (from Fig. 2)	Acquisition dates (month/day/year)		Track	LOS vector: [east, north, up]
	start	end		
a	06/21/1992	07/11/1993	229	[0.397, −0.102 , 0.912]
b	07/26/1992	08/15/1993	229	[0.397, −0.102, 0.912]
c	10/04/1992	09/19/1993	229	[0.397, −0.102, 0.912]
d	10/23/1992	09/03/1993	501	[0.352, −0.0903, 0.932]
e	08/07/1995	08/27/1996	207	[−0.414, −0.106, 0.904]
f	08/08/1995	07/24/1996	229	[0.397, −0.102, 0.912]
g	08/23/1995	10/17/1996	436	[−0.378, −0.0972, 0.921]
h	09/08/1995	09/28/1996	164	[−0.338, −0.087, 0.937]
i	09/11/1995	10/01/1996	207	[−0.414, −0.106, 0.904]
j	09/12/1995	08/28/1996	229	[0.397, −0.102, 0.912]
k	09/27/1995	09/12/1996	436	[−0.378, −0.0972, 0.921]
l	10/01/1995	07/08/1996	501	[0.352, −0.0903, 0.932]
m	10/01/1995	08/12/1996	501	[0.352, −0.0903, 0.932]
n	10/01/1995	07/08/1996	501	[0.352, −0.0903, 0.932]
o	10/02/1995	10/21/1996	501	[0.352, −0.0903, 0.932]
p	07/24/1996	08/13/1997	229	[0.397, −0.102, 0.912]
q	08/13/1997	09/02/1998	229	[0.397, −0.102, 0.912]
r	09/02/1998	09/22/1999	229	[0.397, −0.102, 0.912]

Fig. 4. PFD observations. The white dots outline the assumed limits for the spatial extent of the 1986 PFD. The coastline is derived from the post-1986 DEM. (a) InSAR image spanning the post-emplacement interval 1992–1993 (also shown in Fig. 2a). The grayscale bar on the right identifies the relative displacement toward the satellite, projected onto the LOS vector. Each black-gray-white cycle represents 2.83 cm of relative deformation toward the satellite. (b) Landsat 5 image, TM band 6 (thermal data). The image reveals the lateral extent of the relatively hot (white) PFD and newly emplaced lava with respect to the relatively cold (gray) island. The image acquisition date is April 28, 1986. (c) DEM difference map. The 20 m contour intervals represent differences between the post-1986 DEM and the pre-1986 DEM. Positive and negative thickness contours are white and gray, respectively.

The maximum elevation of the pre-1986 DEM is 1229 m. The 1 : 63,000 Iliamna quadrangle, for which contours were derived from air photos taken in 1957 and was field annotated in 1958, is the source data of the NED pre-1986 eruption DEM for Augustine Volcano. The NED metadata indicate that the contours for the Iliamna quadrangle were most recently updated in 1977. It is unknown whether the contours were updated in part, or as a whole. Therefore, the DEM may portray the topography for multiple dates. Because of this temporal ambiguity, the pre-1986 eruption DEM may also predate the 1976 eruption. For the purposes of this study, we assume this DEM represents the post-1976 topography as suggested by the NED metadata. The post-1986 DEM is constructed entirely from photogrammetric data acquired after the 1986 eruption. The horizontal posting is 10 m with a resolution of 15 m and the RMSE of vertical elevation is less than 15 m (D. Dzurisin, personal comm., 2002). The maximum elevation of this post-1986 DEM is 1250 m.

Both DEMs are resampled to 20 m resolution to match that of the InSAR imagery. The difference between the two DEMs represents the changes in elevation associated with the eruption (Fig. 4c). These changes can be caused by a variety of phenomena, such as volcano-wide deformation due to subsurface processes (e.g., Masterlark and Lu, 2004) and deposition of erupted materials (e.g., Stevens et al., 2001; Lu et al., 2003c). Based on the differences between post- and pre-eruption DEMs, the estimated volume of the PFD is 9.9×10^6 m^3. This estimation assumes the negative thickness (Fig. 4c) is zero. The DEM difference image, with its non-physical negative PFD thickness, presumably indicates the poor quality of the pre-eruptive DEM and justifies the need for a relatively accurate estimate of thickness distribution for the 1986 PDF using the innovative approach proposed in this paper.

4. Method

4.1. Finite element models

FEMs in this study are constructed with the finite element code *ABAQUS* (Hibbet et al., 2003). The code allows for heterogeneous distributions of mate-

rial properties and three-dimensional geometric relationships required for simulating thermoelastic contraction of the cooling PFD. The FEMs solve the four governing equations that describe linear thermoelastic behavior, in terms of coupled excess temperature and displacement, T and u, respectively (Biot, 1956).

All FEMs simulate a thermoelastic PFD embedded in a substrate (Fig. 5). The initially hot PFD contracts as heat flows into the initially cool substrate. Radiant heat transport across the top surface of the PFD is strongly a function of the excess PFD surface temperature, which quickly diminishes during the first few tens of days following emplacement (Patrick et al., 2004). We assume the deformation induced by radiant cooling of the top surface of the PFD is relatively short-lived and becomes insignificant during the post-emplacement interval sampled by the InSAR data. However, this post-emplacement interval is consistent with the time constant (Turcotte and

Table 2
Material properties

Parameter	PFD	Substrate
Young's modulus (Pa)	[a,b]2.5×10^9	[a,b]2.5×10^9
Poisson's ratio (*dimensionless*)	0.25	0.25
Density (kg/m^3)	[c]1650	–
Thermal conductivity (W m^{-1} $^\circ$C^{-1})	[d,e]1.0	–
Specific heat (J kg^{-1} $^\circ$C^{-1})	[a,d]1250	–
Thermoelastic expansion coefficient ($^\circ$C^{-1})	[a]3×10^{-5}	–

[a] (Briole et al., 1997).
[b] (Stevens et al., 2001).
[c] (Begét and Limke, 1989).
[d] (Turcotte and Schubert, 1982).
[e] (Patrick et al., 2004).

Schubert, 1982) associated with contraction of the entire PFD thickness via heat flow into the substrate. The thermoelastic expansion coefficient, thermal conductivity, and specific heat are relatively invariant over a wide range of rocks found near the Earth's surface (Turcotte and Schubert, 1982) and we do not test prediction sensitivities to these parameters. Material properties are summarized in Table 2.

The lateral and bottom boundaries of the model are relatively far away from the PFD and have zero displacement specifications. The top of the model is a free-surface with no heat flow. Nodes at the base of the PFD have $T=0$ specifications for all time, $t(T|_t=0)$. With this configuration, the substrate acts as a simple elastic heat sink. Stated in another way, heat flowing out of the PFD is efficiently transported away from the PFD and out of the system. An efficient groundwater flow system provides a mechanism for this efficient heat transport. This assumption is valid if the time constant for pore fluid flow is much smaller than that for heat flow (Masterlark and Lu, 2004). This is likely to be the case, considering the relatively shallow and localized system beneath the PFD.

The mesh adaptation algorithm, described in Section 4.3, maps the coherent portions of the InSAR image to the nodal positions of an FEM. The adaptation criterion and simulated PFD geometry depend on the coherence distribution. Including the different coherence maps for each InSAR image will most likely cause the algorithm to become unstable. Therefore, we calibrate the deformation models to the
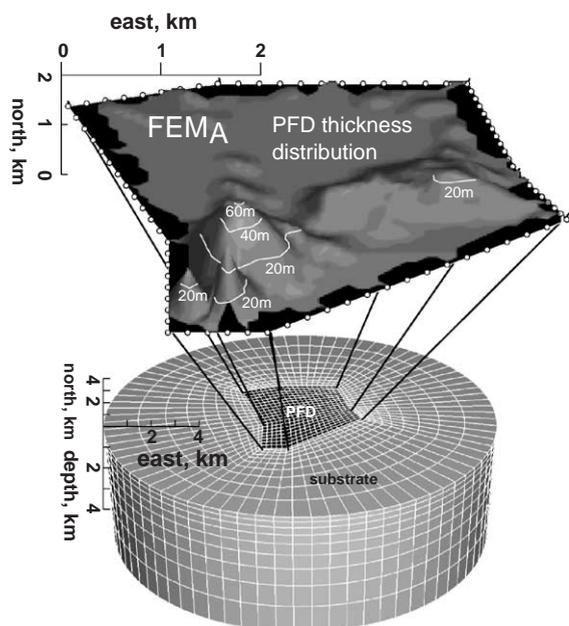

Fig. 5. FEM configuration. The tessellation consists of 12,400 elements and 14,574 nodes. The bottom portion of the figure represents the problem domain, which includes a PFD embedded in the substrate. The shaded relief image in the upper portion of the figure shows an expanded view of the PFD thickness distribution for FEM$_A$. The thickness contour interval is 20 m. Circles outlining the PFD thickness distribution are nodal positions that outline the assumed lateral extent of the PFD.

representative InSAR image shown in Figs. 2a and 4a. This image spans the time interval June 21, 1992 through July 11, 1993. We chose the InSAR image shown in Figs. 2a and 4a for two reasons. First, among the available InSAR images, the chosen image spans a time interval nearest to the 1986 PFD emplacement event (Fig. 3). Thermoelastic deformation decays temporally and an InSAR image spanning a relatively earlier time interval should have a greater deformation signal-to-noise ratio with respect to an image constructed from scenes acquired later on, assuming all InSAR images have constant noise characteristics. Second, implementing phase ramping corrections to the InSAR images will confound the algorithm in its current form. The chosen InSAR image suggests negligible deformation near the margins of the PFD. In this case, we need not correct the deformation for phase ramping (e.g., Masterlark and Lu, 2004). Alternatively, phase ramping corrections would be required, for example, to account for the non-zero deformation along the PFD margins in the InSAR image shown in Fig. 2b. The inability to allow for phase ramping corrections is a limitation of the algorithm presented in this paper. However, the concepts presented in this paper lay the foundations for more complex approaches that may explicitly include multiple InSAR images and phase ramping corrections.

We test the sensitivity to the heat sink configuration by simulating a problem domain having adiabatic conditions. For this FEM, the substrate and PFD are given the same material property specifications. All problem domain boundaries have no heat flow specifications. This model does not include $T|_t = 0$ specifications associated with the heat sink configuration discussed above. Predictions from this model poorly characterize the systematic subsidence of the PFD because the predicted expansion of the heating substrate counteracts the predicted subsidence of the cooling PFD. We therefore reject the adiabatic configuration and assume the substrate acts as a heat sink.

4.2. DEM difference configuration

The first model, FEM$_A$, simulates a PFD having a thickness distribution, **h**, corresponding to the difference between post- and pre-eruption digital elevation models (Figs. 4 and 5). For this configuration, the predicted displacement at time t is a linear function of the initial excess temperature of the PFD, T_0^{PFD}, which we estimate using the linear least-squares inverse solution (Menke, 1989):

$$T_0^{\text{PFD}} = \left[\mathbf{G}^T\mathbf{G}\right]^{-1}\mathbf{G}^T\mathbf{d}^{\text{obs}}. \tag{1}$$

The data kernel, **G**, is a column vector of unit impulse response functions. Each element $\mathbf{G}_j$ is the predicted thermoelastic displacement, due to a unit of initial excess temperature within the PFD, projected onto the LOS vector for nodal position j. The data vector, $\mathbf{d}^{\text{obs}}$, is assembled from the observed LOS displacements. Each element $\mathbf{d}_j^{\text{obs}}$ represents the local LOS displacements interpolated to nodal position j. All nodal positions in **G** and $\mathbf{d}^{\text{obs}}$ correspond to the coherent portions of the InSAR image, excluding the lateral boundaries of the PFD. Positions used to construct **G** and $\mathbf{d}^{\text{obs}}$ are denoted $\mathbf{h}^c$ in Fig. 6. Incoherent nodal positions, $\mathbf{h}^i$, are not populated.

Solving Eq. (1) gives the least-squares estimate for the initial excess temperature, $T_0^{\text{PFD}} = 640 \pm 10$ °C. The root-mean-squared-error (RMSE) between the observed and predicted displacements, $\mathbf{d}^{\text{obs}}$ and $\mathbf{d}^{\text{pre}}$, respectively, is 2.2 cm. Predictions from this model
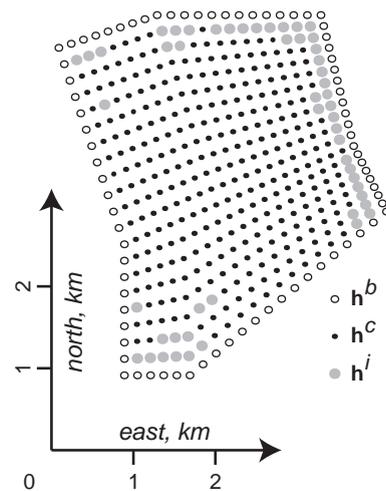

Fig. 6. PFD nodal positions: the free-surface. The open circles, $\mathbf{h}^b$, outline the lateral extent of the PFD (e.g., shown in Fig. 1b). The black and gray circles correspond to nodal positions that lie within the respective coherent and incoherent portions of the InSAR image. Locations for impulse response functions (**G**), displacements ($\mathbf{d}^{\text{obs}}$) and predictions ($\mathbf{d}^{\text{pre}}$) correspond to $\mathbf{h}^c$.

are a significant improvement over the null hypothesis at the 95% confidence level. However, the residual from this model contains systematic errors. A visual inspection of the predictions and residual suggests this model roughly accounts for the observed deformation in the southern and eastern regions of the PFD, where the DEM differences are relatively large (Fig. 7). Conversely, predictions are poor for regions of the PFD where DEM differences are relatively small or zero. This relationship suggests either that *(1)* the thermoelastic deformation mechanism, which is a strong function of the PFD thickness, is inappropriate; *(2)* the thermoelastic model specifications, such as the boundary conditions and material property distributions, poorly approximate the natural system; or *(3)* the thickness distribution of the PFD estimated from the DEM differences contains systematic errors. Field observations (Begét and Limke, 1989) and remote sensing data (Fig. 4b) indicate the PFD was initially hot. Cooling of this initially hot material will induce thermoelastic deformation. The proposed model configurations honor the horizontal geometry of the PFD and the thermoelastic material properties are relatively invariant. The requirement for thermoelastic deformation and the relatively invariant thermoelastic material properties, combined with the prediction misfit versus PFD thickness correlation (Fig. 7), suggest the systematic prediction errors are due to the DEM differences poorly approximating the PFD thickness distribution. Furthermore, the unknown acquisition dates of the pre-1986 eruption DEM introduce uncertainty as to whether or not the DEM elevations are contaminated by materials deposited during the 1976 eruption. This ambiguity suggests the thickness distribution of the PFD estimated with the DEM differences is unreliable and a cause of the misfit.

4.3. PFD thickness: adaptive mesh algorithm

We design three additional models to reduce the systematic prediction errors associated with the a priori PFD thickness distribution and test deformation prediction sensitivities to the initial excess temperature specifications of the PFD. These three models are part of adaptive mesh algorithms that calibrate the predicted thermoelastic deformation, for specified initial excess temperatures, with respect to the observed InSAR image, while iteratively optimizing the PFD thickness distributions. The underlying premise of the algorithm is that the thermoelastic subsidence predicted for a point j at the surface of the PFD is solely a function of the local PFD thickness near point j. The a priori initial excess temperature of the PFD for FEM_B, our preferred model, is 640 °C. This is the initial excess temperature estimation obtained from the least-squares inverse analysis. Computational requirements for each iteration of the adaptive mesh algorithm include model runs for a two-dimensional FEM that solves Laplace's equation and the three-dimensional FEM_B that solves for thermoelastic deformation.

The adaptive mesh algorithm is illustrated in Fig. 8 and described here. The algorithm starts with initial conditions of 1.0 m thickness throughout the PFD ($\mathbf{h}$=1.0); all elements of the incremental thickness vector, δ, are 1.0 m; and the iteration counter, k, is one. The initial thickness of the PFD is set to 1.0 m, rather than zero, because the three-dimensional finite element model requires a finite initial thickness. Thermoelastic deformation of this 1.0 m thick PFD is negligible during 1992–1999. The optimized PFD thickness distributions and volume estimates reported hereafter do not include this initial thickness.

The iterative procedure begins with a Laplacian operator and Dirichlet boundary conditions to estimate the vertical coordinates for nodal positions corresponding to incoherent regions, $\mathbf{h}^i$, for the specified distribution $\mathbf{h}^c$. The finite element approximation of Laplace's equation (Wang and Anderson, 1982) is automatically implemented by constructing a two-dimensional mesh from the horizontal nodal coordinates extracted from the top surface of the PFD portion of FEM_B and imposing the above specifications. Fig. 6 illustrates the nomenclature for $\mathbf{h}$. The three dimensional PFD is constructed by an automated tessellation of the space contained by the flat base and the upper surface, $\mathbf{h}$, of the PFD. The PFD is then automatically embedded into the three-dimensional substrate to update the mesh of FEM_B (Fig. 5).

Thermoelastic displacements are calculated using FEM_B and projected onto the LOS vector to obtain $\mathbf{d}^{pre}$. The thickness $\mathbf{h}_j$, for which predicted subsidence $\mathbf{d}_j^{pre}$ underestimates observed subsidence $\mathbf{d}_j^{obs}$, is increased by δ_j. The thickness $\mathbf{h}_j$ corresponding to a PFD surface node, for which predicted subsidence $\mathbf{d}_j^{pre}$ overestimates observed subsidence $\mathbf{d}_j^{obs}$, is decreased
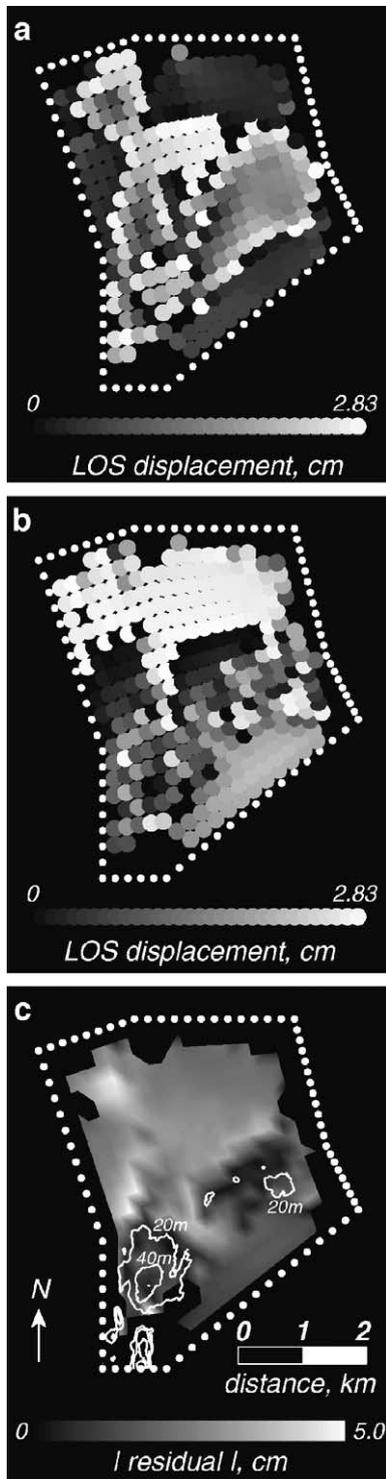
by $\beta\delta_j$, where β is a damping parameter with a value of 0.9 and δ_j is updated to $\beta\delta_j$. This damping stabilizes the iterative procedure. Each iteration increases the maximum thickness by 1.0 m until all subsidence predictions have met or exceeded the observed subsidence values, at which point all elements of δ are less than 1.0 m and k^{stop} is set equal to the number of completed iterations. This produces a PFD thickness distribution that is precise to within 1 m. However, the accuracy of the estimated distribution is somewhat elusive because it depends on the validity of the model and associated assumptions.

5. Results

5.1. Preferred model

For FEM_B and the assumed initial excess temperature, $T_0^{\text{PFD}} = 640$ °C, the adaptive mesh algorithm converges after 126 iterations (Fig. 9). The residual for this model is sub-millimeter (RMSE = 0.3 mm) and the predictions, $\mathbf{d}^{\text{pre}}$, are virtually indistinguishable from the data, $\mathbf{d}^{\text{obs}}$ (Fig. 10). The optimized average thickness, maximum thickness, and volume of the PFD are 9.3 m, 126 m, and 2.1×10^7 m^3, respectively (Fig. 11). The misfit and estimated PFD volume rapidly decrease and increase, respectively, during the first ~50 iterations. The thickness distributions for 50 and 126 iterations are essentially the same. However, the thickness peak near the southwest part of the PFD (Fig. 10c) appears truncated for solutions of 50 versus 126 iterations. With the exception of this thickness peak, the thickness distribution estimated using the adaptive mesh algorithm is within the uncer-

Fig. 7. FEM_A results. (a) Observed displacements. Circles represent the observed displacements interpolated to nodal positions. Relative displacements are shaded according to the grayscale at the bottom. Each black-gray-white cycle represents 2.83 cm of relative deformation toward the satellite. (b) Predicted displacements. Circles represent the predicted nodal displacements due to thermoelastic contraction. Relative displacements are shaded according to the grayscale at the bottom. (c) Absolute residual. The absolute residual distribution inversely correlates to the DEM difference distribution, for which positive values (thickness) are shown with white 20 m contour intervals. Misfit is minimal near regions where the DEM difference distribution suggests significant PFD thickness. However, deformation predictions are poor elsewhere in the problem domain.
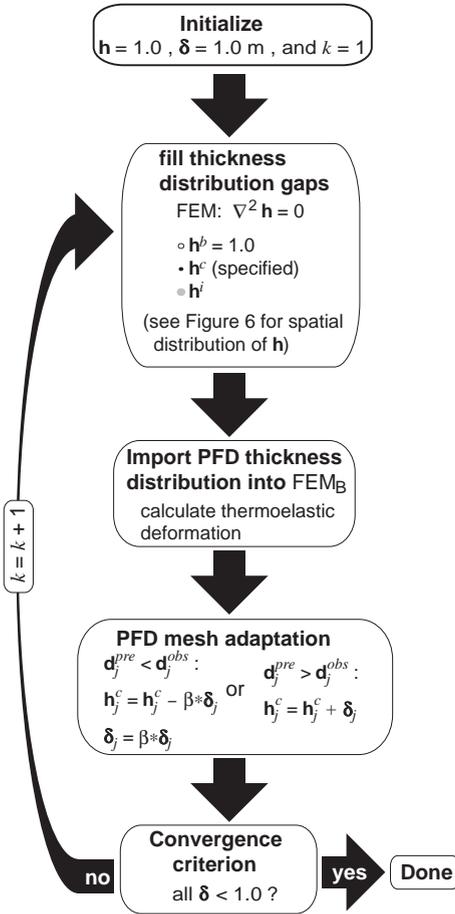
Fig. 8. Adaptive mesh algorithm.

tainty of the DEM difference estimation. This suggests DEMs having much more precise uncertainties, with respect to the two DEMs used in this study, are required to constrain the geometry of the PFD.

Forward modeling predictions indicate the subsidence rate decreases slightly during the temporal window covered by the InSAR images (Fig. 12). These predictions of the transient thermoelastic deformation are qualitatively consistent with the persistent maximum subsidence rate of ~3 cm yr^{-1} suggested by the 18 InSAR images. The predicted displacement for the point overlying the thickest portion of the PFD is almost purely vertical (Fig. 12a). However, the predicted horizontal displacement components are more significant, with respect to the predicted vertical components, along the lateral margins of the PFD.

5.2. Sensitivity to initial excess temperature

The amplitude of the predicted thickness distribution is inversely related to the initial excess temperature of the PFD (Fig. 9). For a given amount of subsidence, a low initial excess temperature requires a relatively thick PFD, whereas a thin PFD is required for a high initial excess temperature. Others suggest PFD emplacement temperatures can range from 400 to 1000 °C (Banks and Hoblitt, 1981) or similarly from 300 to 800 °C (Waythomas and Waitt, 1998). The initial temperature of the PFD is the sum of the
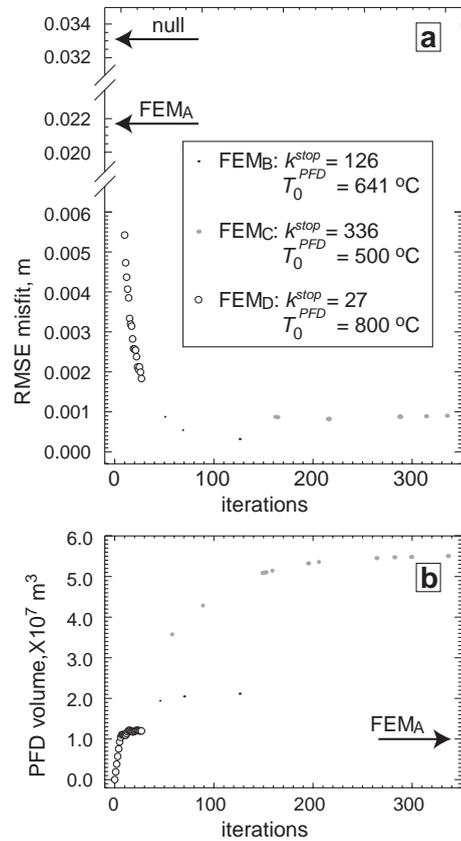

Fig. 9. Iterative evolution of the PFD thickness distribution. (a) Iterative misfit improvement. The misfit decreases rapidly over the first several tens of iterations. The misfits for the null hypothesis and FEM$_A$ are substantially greater than those for FEM$_B$, FEM$_C$, and FEM$_D$. (b) Iterative PFD volume development. The estimated PFD volumes undergo rapid increases over the first several tens of iterations. The PFD volumes estimated using the adaptive mesh algorithm are all greater than that estimated from the DEM difference distribution. The explanation from (a) also applies to (b).
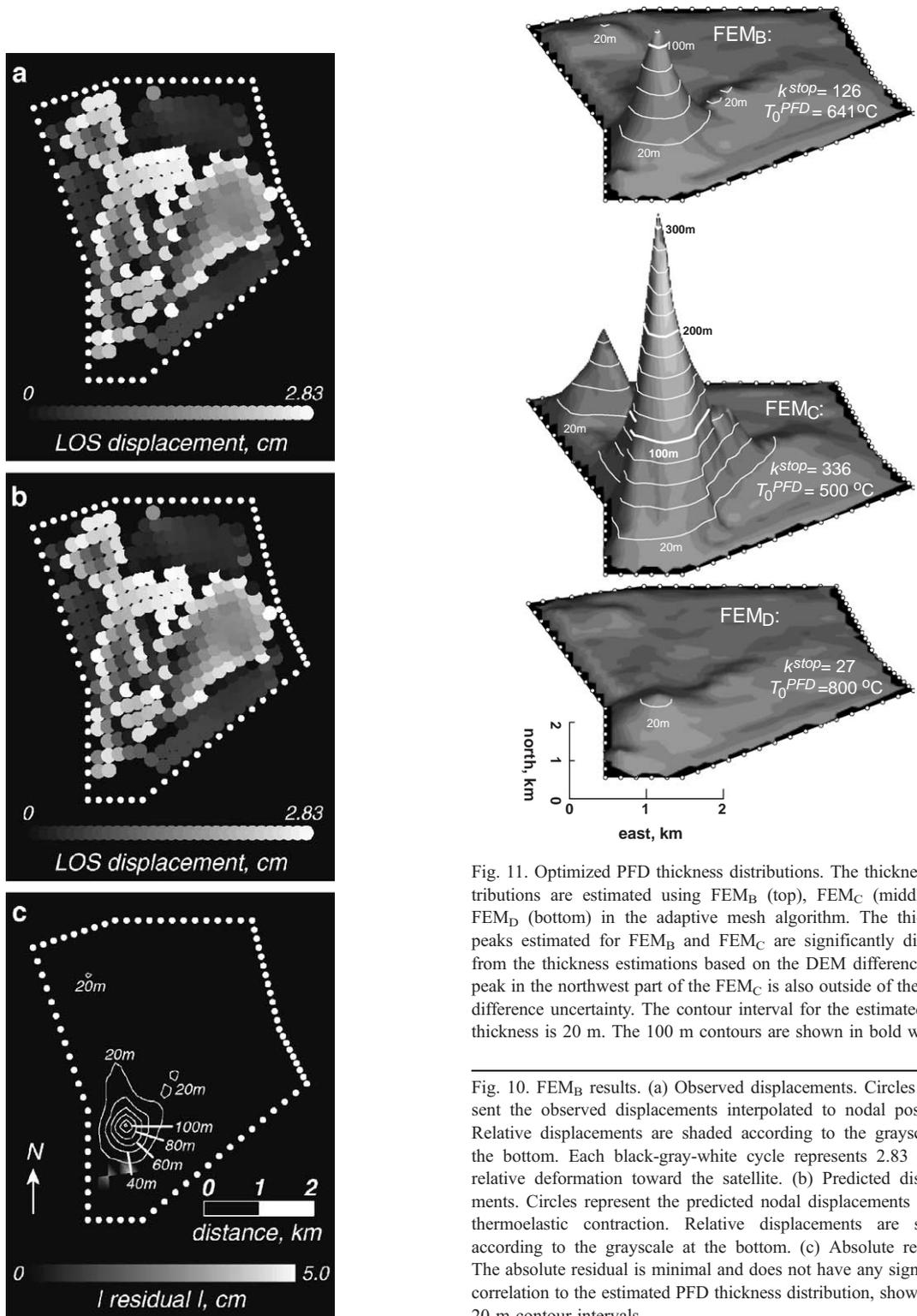
Fig. 11. Optimized PFD thickness distributions. The thickness distributions are estimated using FEM_B (top), FEM_C (middle), or FEM_D (bottom) in the adaptive mesh algorithm. The thickness peaks estimated for FEM_B and FEM_C are significantly different from the thickness estimations based on the DEM difference. The peak in the northwest part of the FEM_C is also outside of the DEM difference uncertainty. The contour interval for the estimated PFD thickness is 20 m. The 100 m contours are shown in bold white.

Fig. 10. FEM_B results. (a) Observed displacements. Circles represent the observed displacements interpolated to nodal positions. Relative displacements are shaded according to the grayscale at the bottom. Each black-gray-white cycle represents 2.83 cm of relative deformation toward the satellite. (b) Predicted displacements. Circles represent the predicted nodal displacements due to thermoelastic contraction. Relative displacements are shaded according to the grayscale at the bottom. (c) Absolute residual. The absolute residual is minimal and does not have any significant correlation to the estimated PFD thickness distribution, shown with 20 m contour intervals.

ambient and initial excess temperatures. Assuming an ambient temperature of ~0 °C (NOAA, 2002), the initial excess temperature determined using FEM_A ($T_0^{PFD} = 640$ °C) is equivalent to the initial emplacement temperature of the PFD and within the expected range of initial emplacement temperatures.

Our estimated initial excess temperature ($T_0^{PFD} = 640$ °C) is in agreement with an in situ field experiment that suggests the initial temperature of the PFD from the 1986 eruption of Augustine Volcano is at least 425 °C (Begét and Limke, 1989). If the initial excess temperature is much less than 640 °C, the thickness of the PFD would have to be much greater than that estimated for both FEM_A and FEM_B. Results from the adaptive mesh algorithm using FEM_C ($T_0^{PFD} = 500$ °C) predict the average thickness of the PFD is 25 m, the maximum thickness is 336 m, and the volume is 5.7×10^7 m^3. These results are unlikely based on the DEM data, particularly for the thickness peak (Fig. 11), and field observations of wave cuts

Table 3
Sensitivity to initial excess temperature

	FEM_A	FEM_B	FEM_C	FEM_D
T_0^{PFD} (°C)	[a]640 ± 10	640	500	800
k^{stop}	–	126	336	27
RMSE (cm)	2.2	0.03	0.09	0.18
h, average (m)	4.3	9.3	25.2	6.2
h, maximum (m)	61	126	336	27
PFD volume (m^3)	9.9×10^6	2.1×10^7	5.7×10^7	1.4×10^7

[a] Least-squares estimation.

that constrain the thickness of the PFD near the northern coast to 1 or 2 m (Begét and Limke, 1989) (Fig. 1b). The PFD thickness predicted using FEM_C is more than 10 m for this coastal location.

Alternatively, FEM_D has a much higher initial excess temperature specification ($T_0^{PFD} = 800$ °C). Results from the adaptive mesh algorithm using this model predict the average thickness of the PFD is 6.2 m, the maximum thickness is 27 m, and the volume is 1.4×10^7 m^3 (Fig. 11). This model estimates the thickness peak in the southwest part of the PFD is much less than the thickness estimated from DEM difference, 61 m. Previous estimations suggest the PFD volume is about 5×10^7 m^3 (Swanson and Kienle, 1988), a value that favors lower initial excess temperatures and a relatively thick PFD. Table 3 summarizes results of FEM_A, FEM_B, FEM_C, FEM_D, and the sensitivity analysis for initial excess temperature. Fig. 11 illustrates the optimal PFD thickness distributions as a function of initial excess temperature.

6. Discussion

6.1. Model limitations

The relatively simple three-dimensional models of thermoelastic deformation reasonably approximate the observed deformation. In order to isolate the effects of the initial excess temperature of the PFD on the thickness distribution estimations, we impose numerous simplifications and assumptions. We assume the substrate is a relatively weak homogeneous material (Table 2) (Briole et al., 1997; Stevens et al., 2001; Lu et al., 2005). This may be an oversimplification of the volcano's structure, which
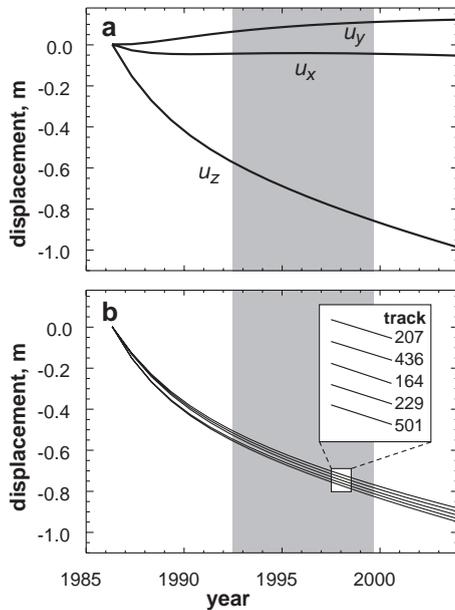

Fig. 12. Transient thermoelastic deformation. We present displacement predictions for the point overlying the thickest portion of the PFD, which is estimated using FEM_B. The gray rectangle shows the interval 1992–1999, during which all curves are relatively linear. (a) Thermoelastic displacement as a function of time for each displacement component. (b) LOS displacement. The three displacement components are projected onto the five different LOS vectors of the InSAR images. Individual curves are labeled in the expanded view.

includes a layered assembly of lava, ash, lahar, avalanche, and PFD materials (Begét and Kienle, 1992; Miller et al., 1998; Waythomas and Waitt, 1998). Although a system of layered materials may be a better approximation for the substrate, this additional structural complexity requires constraining data that is currently unavailable.

We assume the PFD is a homogeneous material, having a uniform initial excess temperature. Field observations suggest the region representing the PFD actually consists of lithic block and ash flow deposits, lithic-rich pumice flow deposits, and lahar deposits (Begét and Limke, 1989). Furthermore, there may be additional depositional gradations within each region. This heterogeneous distribution of material properties suggests a non-uniform initial excess temperature distribution within the PFD. On the other hand, the relatively fast emplacement process of the PFD suggests a homogeneous initial temperature may be appropriate. The lack of sufficient constraining data does not allow us to resolve this issue.

6.2. Other deformation mechanisms

We assume linear thermoelastic behavior is the sole deformation mechanism. Other mechanisms related to the thickness of the PFD, but unrelated to the thermal loading, may also contribute to the observed subsidence. PFDs undergo significant porosity reduction (compaction) following emplacement. The time constant for this process is on the order of hour to days (Rowley et al., 1981), whereas the time constant for thermoelastic contraction is on the order of years (Turcotte and Schubert, 1982). For the purposes of this analysis, we neglect compaction as a deformation mechanism because most of the compaction-related deformation occurs within a short interval following the emplacement. Relatively little thermoelastic deformation occurs during the corresponding interval. Furthermore, the InSAR images document deformation during intervals that begin six years after PFD emplacement and long after the bulk of the PFD compaction.

Transient poroelastic deformation of the substrate is caused by the decay of excess pore fluid pressures initiated by the overlying gravity load of the newly emplaced PFD. The initial response to this loading is undrained and relatively stiff, with respect to the drained conditions, because the pore fluids bear a portion of the load as excess pore fluid pressure (Wang, 2000). As the excess pore fluid pressure decays, the substrate conditions migrate from undrained (stiff) to drained (compliant) conditions and the land surface undergoes subsidence. However, because of the relatively shallow and local flow system associated with this loading, the time constant for the poroelastic response is most likely too small to account for the systematic decadal deformation (Lu et al., 2004).

Transient viscoelastic deformation is caused by the viscous flow of the substrate in response to the gravity load initiated by the emplacement of the PFD. Initially, the substrate behaves as a simple elastic material in response to the gravity load. Viscous flow, which is driven by deviatoric stresses in the substrate, ensues following the initial loading event. The expected time constant for this deformation (Briole et al., 1997; Stevens et al., 2001; Lu et al., 2004) is of the same order as that for thermoelastic deformation and suggests the observed subsidence may be caused, in part, by viscoelastic relaxation. It is difficult to conclusively predict the effects of viscoelastic relaxation based on the available constraining data. This deformation mechanism is also a function of the PFD thickness distribution. Investigations of deforming lava flows (Lu et al., 2004) suggest the magnitude of viscoelastic deformation is a few tens-of-percent of that for thermoelastic relaxation.

Thermoelastic deformation alone can account for the observed deformation and is consistent with the thermal information derived from field observations (Begét and Limke, 1989) and remote sensing data (Fig. 4b). Viscoelastic deformation may account for the observed subsidence, but it cannot account for the thermal observations (Begét and Limke, 1989) and the thermal anomaly shown in Fig. 4b. It is likely that the observed deformation is the result of some combination of thermoelastic and viscoelastic mechanisms, but we cannot resolve the relative contributions from each without further constraining data. Interestingly, all of the alternative deformation mechanisms suggested above will increase the deformation rate. Therefore, thickness distributions and initial temperature estimations represent upper bounds, rather than actual estimations.

6.3. Mesh adaptation

Mesh construction has historically been a labor-intensive component of constructing three-dimensional FEMs of geomechanical systems. Computational simplicity is often cited to justify oversimplified models of deformational systems, particularly for inverse analyses (Masterlark, 2003). The validity of many assumptions associated with the FEMs and mesh adaptation algorithm used in this study is arguable. However, the excellent agreement of displacement observations and predictions demonstrates the success of the mesh adaptation algorithm introduced in this study, which can automatically optimize the geometric configuration of an FEM. If available, high quality pre- and post-event digital elevation models can precisely constrain the vertical geometric components of a newly emplaced material (Stevens et al., 2001; Lu et al., 2003c). In that case, an adaptive mesh algorithm is unnecessary. The value of the adaptive mesh algorithm lies in applications for which geometric constraining data are lacking, as is the case for the PFD emplaced during the 1986 eruption of Augustine Volcano.

7. Conclusions

Thermoelastic deformation predictions, subject to an assumed a priori PFD thickness distribution, contain systematic errors and poorly approximate the observed deformation. Accurate simulation of post-emplacement deformation of the PFD due to thermoelastic contraction requires an accurate estimation of the PFD thickness distribution. The proposed method combines InSAR data, FEMs, and an adaptive mesh algorithm to generate optimized thickness distribution maps of the PFD emplaced during the 1986 eruption of Augustine Volcano. The preferred model (FEM_B), which is used in the proposed method, suggests thermoelastic contraction is a plausible mechanism to account for the observed subsidence of the PFD. Displacement predictions from this model are remarkably consistent with observations.

FEMs are powerful tools that allow us to simulate a wide variety of complex geomechanical systems having a priori geometric specifications. Reconfiguring the mesh of an FEM can be labor-intensive and is a significant drawback to geome-

chanical applications of FEMs. This study demonstrates a method that automatically performs iterative mesh reconfigurations, which can greatly reduce misfit attributed to an a priori geometric configuration. Further development of these methods may allow investigators to do away with many of the restrictive model assumptions and oversimplified configurations typically invoked for operational and computational simplicity.

Appendix A. Symbols

d	vector, LOS displacements
G	vector, unit impulse response functions
h	vector, thickness distribution
j	nodal position index
k	iteration index
T	time
T	excess temperature
T_0^{PFD}	initial excess temperature of PFD
u	displacement
δ	vector, incremental thickness distribution

References

Banks, N.G., Hoblitt, R.P., 1981. Summary of temperature studies of 1980 deposits. In: Lipman, P.W., Mullineaux, D.R. (Eds.), The 1980 Eruptions of Mount St. Helens, Washington, U.S. Geological Survey Professional Paper, vol. 1250, pp. 295–313.

Begét, J.E., Kienle, J., 1992. Cyclic formation of debris avalanches at Mount St Augustine volcano. Nature 356, 701–704.

Begét, J.E., Limke, A.J., 1989. Density and void ratio on emplacement of a small pyroclastic flow, Mount St. Augustine, Alaska. Journal of Volcanology and Geothermal Research 39, 349–353.

Biot, M.A., 1956. Thermoelasticity and irreversible thermodynamics. Journal of Applied Physics 27, 240–253.

Briole, P., Massonnet, D., Delacourt, C., 1997. Post-eruptive deformation associated with the 1986–87 and 1989 lava flows of Etna detected by radar interferometry. Geophysical Research Letters 24, 37–40.

Gesch, D., 1994. Topographic data requirement for EOS global change research. USGS Open-File Report, 94–62.

Gesch, D., Oimoen, M., Greenlee, S., Nelson, C., Steuck, M., Tyler, D., 2002. The national elevation dataset. Photogrammetric Engineering and Remote Sensing 68, 5–11.

Hibbet, Karlsson, and Sorensen, Inc., 2003. ABAQUS, version 6.4, http://www.hks.com.

Lipman, P., Moore, J.G., Swanson, D.A., 1981. Bulging of the north flank before the May 18 eruption—geodetic data. In: Lipman, P.W., Mullineaux, D.R. (Eds.), The 1980 Eruptions of Mount St. Helens, Washington, U.S. Geological Survey Professional Paper, vol. 1250, pp. 143–155.

Lu, Z., Masterlark, T., Power, J., Dzurisin, D., Wicks Jr., C., Thatcher, W., 2002. Subsidence at Kiska volcano, western Aleutians, detected by satellite radar interferometry. Geophysical Research Letters 29, 1855. doi: 10.1029/2002GL014948.

Lu, Z., Masterlark, T., Dzurisin, D., Rykhus, R., Wicks Jr., C., 2003a. Transient inflation rate detected with satellite interferometry and its implication to the plumbing system at Westdahl volcano, Alaska. Journal of Geophysical Research 108, 2354. doi: 10.1029/2002JB002311.

Lu, Z., Wicks Jr., C., Dzurisin, D., Power, J., Thatcher, W., Masterlark, T., 2003b. Interferometric synthetic aperture radar studies of Alaska volcanoes. Earth Observation Magazine 12, 8–18.

Lu, Z., Fielding, E., Patrick, M., Trautwein, C., 2003c. Estimating lava volume by precision combination of multiple baseline spaceborne and airborne interferometric synthetic aperture radar: the 1997 eruption of Okmok volcano, Alaska. IEEE Transactions on Geoscience and Remote Sensing 41, 1428–1436.

Lu, Z., Masterlark, T., Dzurisin, D., 2005. Interferometric synthetic aperture radar study of Okmok volcano, Alaska, 1992-2003: magma supply dynamics and postemplacement lava flow deformation. Journal of Geophysical Research 110, B02403. doi: 10.1029/2004JB003148.

Massonnet, D., Feigl, K., 1998. Radar interferometry and its application to changes in the Earth's surface. Reviews of Geophysics, 441–500.

Massonnet, D., Rossi, M., Carmona, C., Adragna, F., Peltzer, G., Feigl, K., Rabaute, T., 1993. The displacement field of the Landers earthquake mapped by radar interferometry. Nature 364, 138–142.

Masterlark, T., 2003. Finite element model predictions of static deformation from dislocation sources in a subduction zone: Sensitivities to homogeneous, isotropic, and Poisson-solid, and half-space assumptions. Journal of Geophysical Research 108, 2540. doi: 10.1029/2002JB002296.

Masterlark, T., Lu, Z., 2004. Transient volcano deformation sources imaged with interferometric synthetic aperture radar: application to Seguam Island, Alaska. Journal of Geophysical Research 109, B01401. doi: 10.1029/2003JB002568.

Menke, W., 1989. Geophysical Data Analysis: Discrete Inverse Theory. International Geophysical Series, vol. 45. Academic Press, Inc., San Diego.

Miller, T.P., McGimsey, R.G., Richter, D.H., Riehle, J.R., Nye, C.J., Yount, M.E., Dumoulin, J.A., 1998. Catalog of the historically active volcanoes of Alaska. US Geological Survey Open-File Report 98-0582.

NOAA, 2002. Climatography of the United States No. 85, http://www.ncdc.noaa.gov/climatenormals/clim85/CLIM85_TEMP01.pdf, Ashville, NC.

Patrick, M.R., Dehn, J., Dean, K., 2004. Numerical modeling of lava cooling applied to the 1997 Okmok eruption: approach and analysis. Journal of Geophysical Research 109, B03202. doi: 10.1029/2003JB002537.

Pauk, B.A., Power, J.A., Lisowski, M., Dzurisin, D., Iwatsubo, E.Y., Melbourne, T., 2001. Global positioning system (GPS) survey of Augustine volcano, Alaska, August 3–8, 2000: Data processing, geodetic coordinates and comparison with prior geodetic surveys. US Geological Survey Open-File Report 01-0099.

Peltzer, G., Rosen, P., Rogez, F., Hudnut, K., 1996. Postseismic rebound in fault step-overs caused by pore-fluid flow. Science 273, 1202–1204.

Pollitz, F.F., Wicks, C., Thatcher, W., 2001. Mantle flow beneath a continental strike-slip fault: postseismic deformation after the 1999 Hector Mine earthquake. Science 293, 1814–1818.

Rowley, P.D., Kuntz, M.A., Macleod, N.S., 1981. Pyroclastic-flow deposits. In: Lipman, P.W., Mullineaux, D.R. (Eds.), The 1980 Eruptions of Mount St. Helens, Washington, U.S. Geological Survey Professional Paper, vol. 1250, pp. 489–512.

Sabins, F.F., 1997. Remote Sensing Principles and Interpretation, 3rd edition. W.H. Freeman and Company, New York.

Simkin, T., Siebert, L., 1994. Volcanoes of the World. Geoscience Press, Tucson. 349 pp.

Stenoien, M.D., Bentley, C.R., 2000. Pine island glacier, Antarctica: a study of the catchment using interferometric synthetic aperture radar measurements and radar altimetry. Journal of Geophysical Research 105, 21761–21780.

Stevens, N.F., Wadge, G., Williams, C.A., Morely, J.G., Muller, J.-P., Murray, J.B., Upton, U., 2001. Surface movements of emplaced lava flows measured by synthetic aperture radar interferometry. Journal of Geophysical Research 106, 11293–11313.

Swanson, S.E., Kienle, J., 1988. The 1986 eruption of Mount St. Augustine: field test of a hazard evaluation. Journal of Geophysical Research 93, 4500–4520.

Turcotte, D.L., Schubert, G.J., 1982. Geodynamics: Applications of Continuum Physics to Geological Problems. John Wiley & Sons, New York.

Wang, H.F., 2000. Theory of Linear Poroelasticity: with Applications to Geomechanics. Princeton University Press, Princeton.

Wang, H.F., Anderson, M.P., 1982. Introduction to Groundwater Modeling: Finite Difference and Finite Element Methods. Academic Press, San Diego.

Waythomas, C.F., Waitt, R.B., 1998. Preliminary volcano-hazard assessment for Augustine volcano, Alaska. USGS Open-File Report 98–106.